Robotica: (2021) volume 39, pp. 165–180. © The Author(s), 2020. Published by Cambridge University Press
doi:10.1017/S0263574720000740

Design and Function Realization of Nuclear Power Inspection Robot System

Zhang Zhonglin*, Fu Bin, Li Liquan and Yang Encheng

College of Mechanical and Electrical Engineering, Harbin Engineering University, Harbin 150001, China.
E-mails: 974507911@qq.com, liliquan@hrbeu.edu.cn, yangencheng@hrbeu.edu.cn

(Accepted August 1, 2020. First published online: September 4, 2020)

SUMMARY
The particularity of nuclear power plant environment requires that the nuclear power inspection robot must be remote control operation. The main purpose of the inspection robot is to carry out inspection, prevention, reporting, and safety emergency operation on the instruments, so as to provide guarantee for the safe operation of the nuclear power plant. Based on the representative configuration of nuclear power robot at home and abroad, this paper develops a small and lightweight nuclear power plant inspection robot, including walking mechanism, lifting mechanism, operating mechanism, image acquisition, information communication and control system, etc., to carry on the statics analysis to the key components of the inspection robot and verify that the stiffness and strength of the mechanical structure meet the requirements of lightweight design. Modal analysis is carried out to verify that the motor does not cause resonance when working. The kinematic model of the robot has been established and can provide the theoretical basis for the controller design. A hierarchical control system based on LabVIEW upper computer monitoring and control operation interface is established, which uses adaptive fuzzy Proportional Integral Derivative (PID) control to simulate the walking control, and then realizes the control of walking mechanism through software programming, and the adaptive fuzzy PID control has better effect than the conventional PID control. The S-type acceleration and deceleration algorithm is used to realize the accurate control of the position location of the lifting mechanism. Finally, combined with the experiment of 5MS robot comprehensive experimental platform, it is proved that the inspection robot can realize remote control function operation.

KEYWORDS: Nuclear power inspection robot; Structural analysis; Modal analysis; Robot kinematics; Fuzzy PID control; LabVIEW upper computer; 5MS (5-joint manipulator system).

1. Introduction

Nuclear energy as a new way of clean energy has been widely used in many countries around the world, despite the high safety and reliability of nuclear power plants, but in the past a number of nuclear accidents have caused heavy human losses and serious damage to the ecological environment (There are seven levels of nuclear accidents, the higher the level, the greater the hazard.), such as the Three Mile Island nuclear accident (Level 5) on March 28, 1979, the explosion at the fourth reactor of the Chernobyl nuclear power plant in the former Soviet Union on April 26, 1986 (Level 7), and the leak at the first nuclear power plant in Fudao, Japan, on April 11, 2011 (Level 6). The damage of nuclear radiation to human beings is fatal, so it is of great significance and value for nuclear power plant inspection robot as an important executor to carry out inspection and operation tasks in the nuclear power environment as a substitute person.[1,2]

Several countries have developed nuclear power robots (in Fig. 1). Robot SURBOT (1987), developed by Remotec, USA, HAZBOT (1990), developed by the California Institute of Technology,

* Corresponding author. E-mail: zhangzhonglin@hrbeu.edu.cn

https://doi.org/10.1017/S0263574720000740 Published online by Cambridge University Press

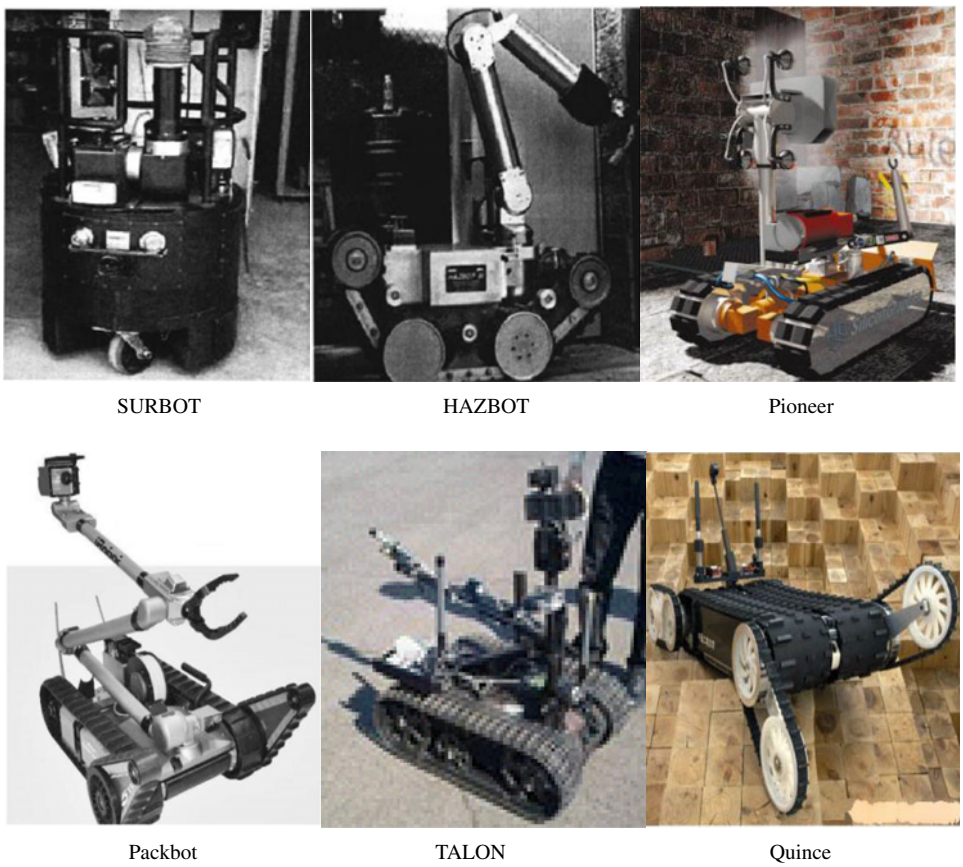


Fig. 1. Design cases of nuclear power inspection robots.

Pioneer (1998), developed by NASA, and the Energy Bureau, in 2011, the PackBOT developed by iROBOT of Japan, the TALON developed by QinetiQ, and the Quince developed by Chiba Institute of Technology and International Rescue System Research Institute of Northeastern University, Japan, which are used for the detection and monitoring of nuclear power operations facilities,[3,4] the prevention of early warning, Nuclear power environmental detection,[5] and so on.

These nuclear power robots are analyzed from the functional configuration, which are equipped with visual remote monitoring equipment, walking mechanism, multi-joint manipulator, or sampling operation tools. Drawing on the experience of nuclear power inspection robot,[6–8] this paper uses modular design and hierarchical control method to develop a nuclear power inspection robot.

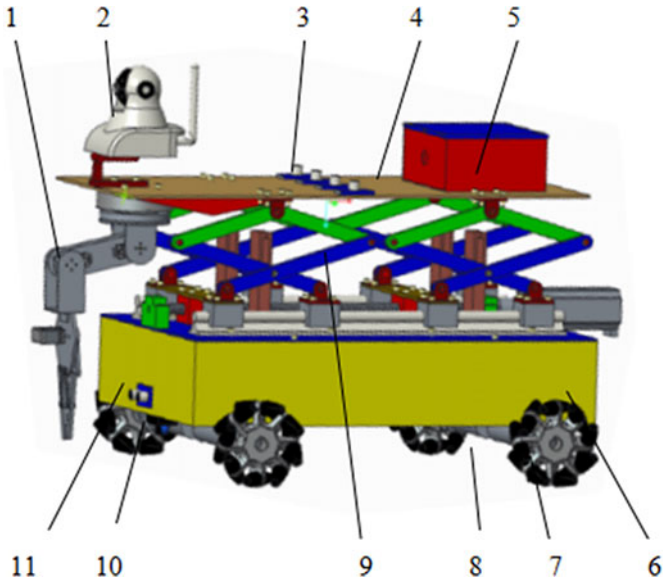
2. Robot Design and Analysis

The nuclear power inspection robot has main functions including robot walking, visual inspection, valve opening and closing, remote control operation, and other equipment can be equipped to achieve added functions.

Based on the nuclear power inspection, robot should have flexible motion ability and increase the detection height and operating range to complete the daily inspection work content requirements, its main components include walking mechanism, lifting mechanism, operating mechanism, video monitoring module and sensor module, etc., and the overall design of the system is shown in Fig. 2.

In the course of carrying out the task, the Mcnum wheel provides the moving driving force of the robot system, moving to the target position, and the driving force of the lifting mechanism is provided by the stepper motor, which enables the acquisition operation platform to realize the lifting movement and widen the longitudinal range of the image acquisition, and the manipulator can perform such operations as valve tightening, picking matter, etc. The video acquisition module and sensor on the acquisition operation platform are monitored and detected in real time, and the alarm information is sent to the upper computer when an anomaly is found.

https://doi.org/10.1017/S0263574720000740 Published online by Cambridge University Press



1-Manipulator 2-Image Acquisition Module 3-Sensor 4-Acquisition Operation Platform 5-Sensor Acquisition Box 6-Control Box 7-Mcnum Wheel 8-DC Deceleration Motor 9-Lifting Mechanism Module 10-Tracing Module 11-Ultrasonic Ranging Module

Fig. 2. Design diagram of nuclear power inspection robot.

2.1. Establishment of basic mechanics equations

Based on the structure design of nuclear power inspection robot, due to the symmetrical distribution structure of four four-bar lifting mechanisms, the force can be analyzed by analyzing a single four-bar mechanism, and the force model is simplified as shown in Fig. 3.

The torque at point $A1$ equals zero, which is as follows:

$$F_{G1} \times L_{A1} + F_{A2} \times (L_{A2} + L_{A3}) = F_{G2} \times L_{A2} + F_{G3} \times (L_{A2} + L_{A3} + L_{A4}) \tag{1}$$

The torque at point $A2$ equals zero, which is as follows:

$$F_{G1} \times (L_{A1} + L_{A2} + L_{A3}) + F_{G2} \times L_{A3} = F_{A1} \times (L_{A2} + L_{A3}) + F_{G3} \times L_{A4} \tag{2}$$

Based on Eqs. (1) and (2), and $F_{A1} = F_{A2} = F_A$, thus, F_A is computed.

Based on the force equilibrium equation, we compute the following equations:

$$\begin{cases} F_A + m_1 g + m_2 g + m_3 g + m_4 g = F_{Ey} + F_G \\ F_{Ex} = F_D \end{cases} \tag{3}$$

$$F_{AB} = \frac{F_A}{2\cos(90^\circ - \theta)} = \frac{F_A}{2\sin\theta} \tag{4}$$

The torque at point B equals zero, which is as follows:

$$\begin{cases} F_{Bx} - F_{AB}\cos\theta = 0 \\ F_{AB}\sin\theta + m_1 g - F_{By} - F_{m_1 A} = 0 \\ m_1 g\cos\theta \cdot \dfrac{l_{AB}}{2} - F_{m_1 A}\cos\theta \cdot l_{AB} = 0 \end{cases} \tag{5}$$

Therefore,

$$\begin{cases} F_{Bx} = F_{AB}\cos\theta = \dfrac{F_A}{2\sin\theta} \\ F_{m_1 A} = \dfrac{m_1 g\cos\theta \cdot \dfrac{l_{AB}}{2}}{\cos\theta \cdot l_{AB}} = \dfrac{m_1 g}{2} \end{cases} \tag{6}$$

https://doi.org/10.1017/S0263574720000740 Published online by Cambridge University Press

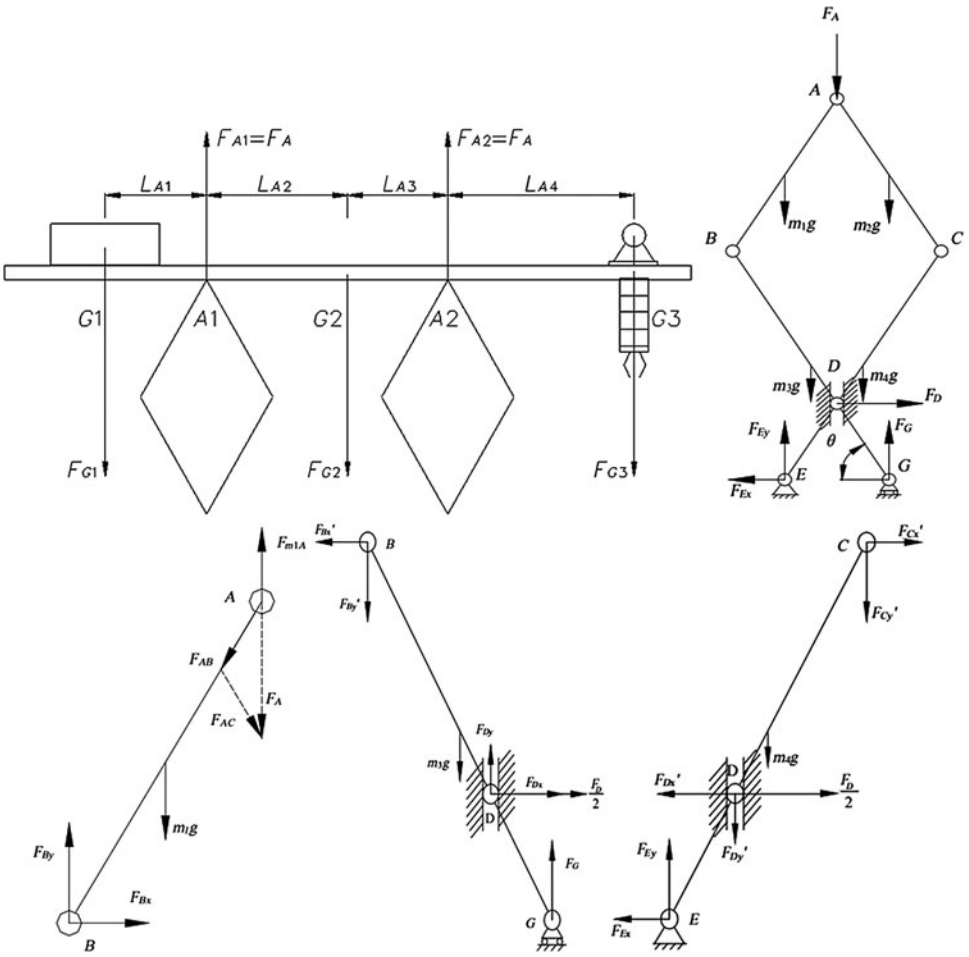


Fig. 3. Force analysis of four-bar mechanism.

Substituting F_{AB} and F_{m1A} into Eq. (6), we get the following equations:

$$F_{By} = F_{AB}\sin\theta + m_1 g - F_{m_1 A} = \frac{F_A}{2\sin\theta}\sin\theta + m_1 g - \frac{m_1 g}{2} = \frac{F_A + m_1 g}{2} \tag{7}$$

Equations (8) and (9) can be simultaneously obtained, which are as follows:

$$\begin{cases} F_{Dx} + \dfrac{F_D}{2} = F_{Bx}{}' = \dfrac{F_A}{2\sin\theta} \\ F_{Dy} = \dfrac{(F_A + (F_A + m_1 g)\cos\theta + m_3 g)\, l_{BG} - F_A l_{DG}}{2 l_{DG}\cdot\cos\theta} \\ F_G = \dfrac{((F_A + m_1 g + 2m_3 g)\cos\theta + F_A)\, l_{DG} - (F_A + (F_A + m_1 g)\cos\theta + m_3 g)\, l_{BG}}{2 l_{DG}\cdot\cos\theta} \end{cases} \tag{8}$$

$$\begin{cases} F_{Ey} = \dfrac{((F_A + m_2 g + 2m_4 g)\cos\theta - F_A)\, l_{DG} + (F_A + (F_A + m_1 g)\cos\theta + m_3 g)\, l_{BG}}{2 l_{DG}\cdot\cos\theta} \\ F_{Ex} = -\dfrac{F_A \cdot l_{CD} + (F_A + m_2 g)\cos\theta \cdot l_{CD} + 2m_4 g\left(\dfrac{l_{CE}}{2} - l_{DE}\right)}{2\sin\theta \cdot l_{DE}} \\ \qquad \dfrac{(F_A + m_2 g + 2m_4 g)\cos\theta - F_A}{2\sin\theta} - \dfrac{(F_A + (F_A + m_1 g)\cos\theta + m_3 g)\, l_{BG}}{2\sin\theta \cdot l_{DG}} \end{cases} \tag{9}$$

https://doi.org/10.1017/S0263574720000740 Published online by Cambridge University Press

Table I. The parameters values.

$m_1g = m_2g$ (N)	$m_3g = m_4g$ (N)	$l_{CE} = l_{BG}$ (mm)	$l_{DE} = l_{DG}$ (mm)	$l_{AB} = l_{CD}$ (mm)	F_b(N)	F_d(N)	F_{Ab}	F_{Ad}	Mg(N)
0.883	1.215	225	75	150	39.4	3.65	19.7	1.825	24.235

The parameter values used are in Table I. Based on the actual load of the acquisition operation platform, the force of the four-bar mechanism at point b is as follows:

$$F_{Gb} = \frac{-3228.375 - 2897.7\cos\theta}{150\cos\theta} \quad F_{Exb} = -\frac{6304.5 + 9422.1\cos\theta}{150\sin\theta}$$

$$F_{Db} = F_{Exb} = -\frac{6304.5 + 9422.1\cos\theta}{150\sin\theta} \quad F_{Eyb} = \frac{6342.15\cos\theta + 3228.375}{150\cos\theta}$$

Similarly, the force of the four-bar mechanism at point d would be as follows:

$$F_{Gd} = \frac{-547.125 - 216.45\cos\theta}{150\cos\theta} \quad F_{Exd} = -\frac{912 + 1378.35\cos\theta}{150\sin\theta}$$

$$F_{Dd} = F_{Exd} = -\frac{6304.5 + 9422.1\cos\theta}{150\sin\theta} \quad F_{Eyd} = \frac{979.65\cos\theta + 547.125}{150\cos\theta}$$

In the actual work to determine the working angle θ range is 17.058°−63.295°. Thus, the extremum of G-point force and E-point force is calculated and loaded into the finite element model of the structure, and the force analysis can be carried out.

2.2. The static analysis of the key structural components

In the selection of structural materials, 40 profiles of light metal materials with high solderability and good mechanical properties are selected. In ANSYS Workbench, the static analysis of the key components of the robot is carried out by means of finite element calculation, in order to ensure the reliability of the operation of the nuclear power inspection robot. The 3D model is imported into ANSYS Workbench, and the structure statics analysis is carried out after meshing and boundary condition constraint,[9] and the results are shown in Fig. 4.

Based on the calculation results, the maximum displacement deformation occurs at the top of the left four-bar mechanism, and its maximum deformation displacement is 0.10006 mm, so the ratio of the maximum deformation displacement and the total stroke is $\delta = \frac{0.10006}{112.5} = 0.089\%$, and the maximum principal stress is 6.3266 MPa, which occurs at the intersection of the longer two bars of the four-bar mechanism, and the yield limit of 40 profile aluminum is 150–190 MPa to meet strength requirements.

2.3. Modal analysis

In order to avoid the resonance phenomenon of the mechanism, in ANSYS, the modal analysis of the four-bar lifting mechanism is carried out in the course of the mechanism motion with the generation of vibration.[10,11] The first six-order mode shapes are shown in Fig. 5(a), (b), (c), (d) (e), (f), according to the results in Fig. 5, and the features of the natural frequency mode shapes of each order are listed in Table II.

Based on calculation, the each order excitation frequencies of the excitation source stepper motor of the system are 2, 4, 6, 8, 10, and 12 Hz, respectively, and the frequencies obtained are much smaller than the frequency of modal analysis, and the structure does not resonate with the excitation frequency of the motor, which indicates that it meets the design requirements.

3. The Kinematic Analysis of the Robot

The motion law of Mcnum wheel is analyzed, and the kinematics equation and inverse kinematics equation of Mcnum wheel chassis are obtained from the model of one wheel to the whole four wheels. The motion model of four-bar lifting mechanism is established, and the relationship between the motion hinge point and the four-bar lifting mechanism and the relationship equation

https://doi.org/10.1017/S0263574720000740 Published online by Cambridge University Press

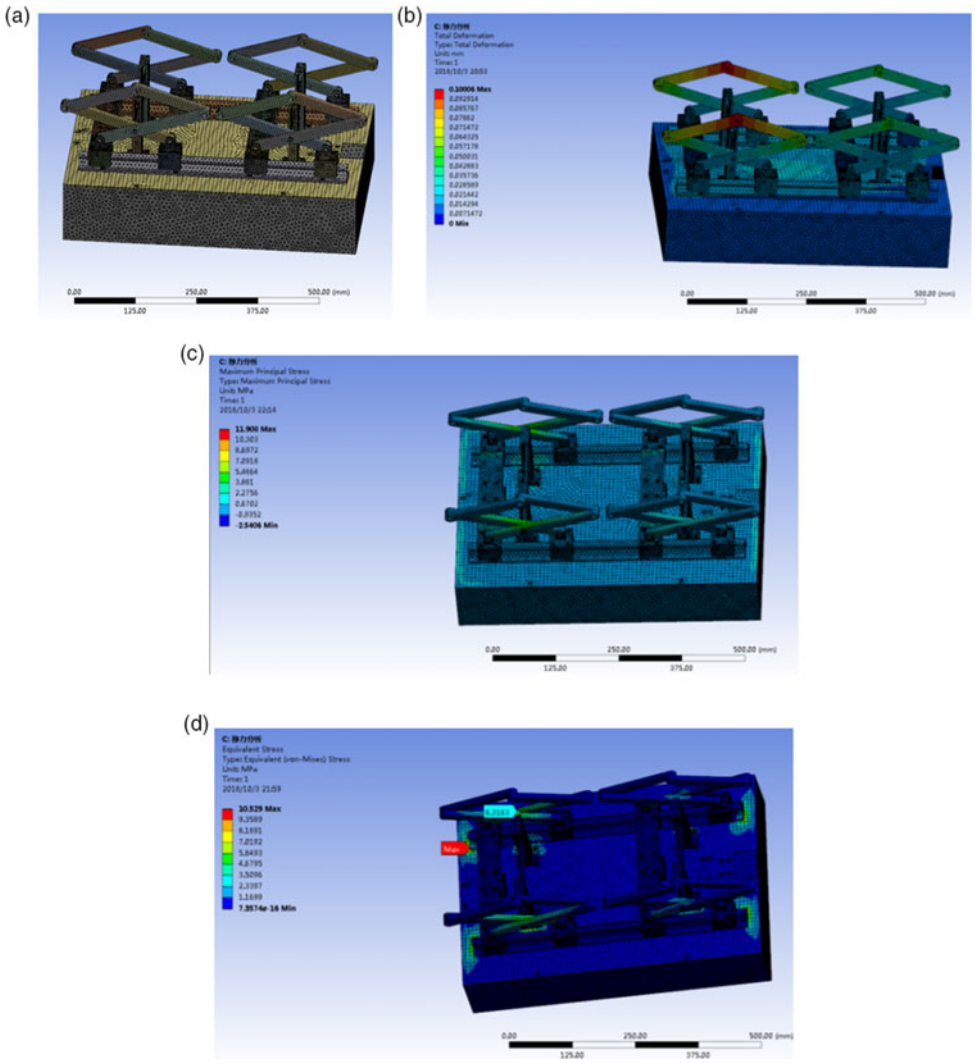


Fig. 4. Analysis of robot structure statics. (a) Meshing result. (b) Deformation analysis results. (c) Maximum principal stress analysis results. (d) Results of equivalent stress analysis.

between the driving motor speed and the lifting speed are obtained. The manipulator (5MS) D-H model is established to obtain the positive kinematics expression of the T matrix of the joint, and the inverse kinematics solution of the manipulator is obtained according to the geometrical quantity of the manipulator.

The Mcnum wheel is the core of the entire nuclear power inspection robot to carry out the trajectory of the inspection task,[12,13] and its structure diagram is shown in Fig. 6(a).

The *O-XY* coordinate is the robot body moving coordinate, and the *O* point is located at the intersection of four Mcnum wheel connection centers and the plane where the central axis is located. The $o_1 - x_1y_1$ coordinate is the local coordinate of Mcnum wheel 1, and ω_1, ω_2, ω_3, and ω_4 are the angular velocity of wheel 1, wheel 2, wheel 3, and wheel 4, respectively, that is, the motor output angular velocity, ω_o is the angular velocity of robot body around the coordinate origin *O*, rad/s; $2a$ is the distance of the center of the Mcnum wheel in the *X* direction and $2b$ is the distance of the center axis of the Mcnum wheel in the *Y* direction. v_{g1} and v_{r1} are the tangential speed of the Mcnum wheel 1 roll and the ground contact surface relative to the roller shaft and the tangential speed of the Mcnum wheel 1 effective radius *R* relative to the hub axis, respectively, m/s, which are decomposed into *X*1 axis and *Y*1 axis of the local coordinate.

$$\begin{bmatrix} v_{1x} \\ v_{1y} \end{bmatrix} = \begin{bmatrix} 0 & -\sin\beta \\ R & \cos\beta \end{bmatrix} \begin{bmatrix} \omega_1 \\ v_{g1} \end{bmatrix} \tag{10}$$

https://doi.org/10.1017/S0263574720000740 Published online by Cambridge University Press

Table II. Analysis of each order mode shape for four-bar lifting mechanism.

Modal order	Modal frequency/Hz	Total deformation/mm	Mode shape features
First order	104.3	22.397	The four-bar lifting mechanism produces a certain offset in the z direction and has a certain deflection around the x-axis, so that the mechanism produces a certain left and right tilt
Second order	110.04	31.873	The deformation of the mechanism occurs in the negative direction along the z axis of the support bottom, which is not related to the four-bar lifting mechanism and has little effect on the mechanism
Third order	118.74	20.181	The four-bar lifting mechanism only produces an offset in the z direction, resulting in upper and lower vibrations
Fourth order	137.64	27.491	The four-bar lifting mechanism produces a certain offset in the z direction and has a certain bending compression around the diagonal direction
Fifth order	147.25	25.839	The four-bar lifting mechanism produces a certain offset in the z direction and has a certain deflection around the y axis, which causes the mechanism to produce a certain amount of front and rear tilt
Sixth order	161.41	22.573	Similar to the first order, the deflection of the base around the x-axis is larger than that of the first order and the offset of the four-bar lifting mechanism along the y axis is also greater

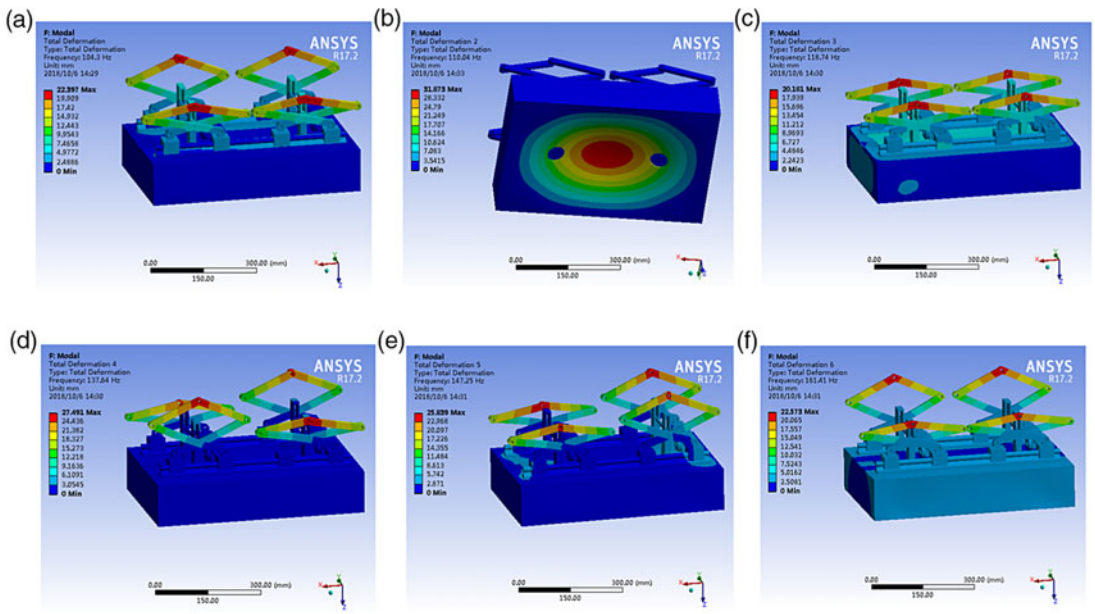


Fig. 5. The first six-order mode shapes of the four-bar lifting mechanism. (a) First-order mode shape. (b) Second-order mode shape. (c) Third-order mode shape. (d) Fourth-order mode shape. (e) Fifth-order mode shape. (f) Sixth-order mode shape.

https://doi.org/10.1017/S0263574720000740 Published online by Cambridge University Press

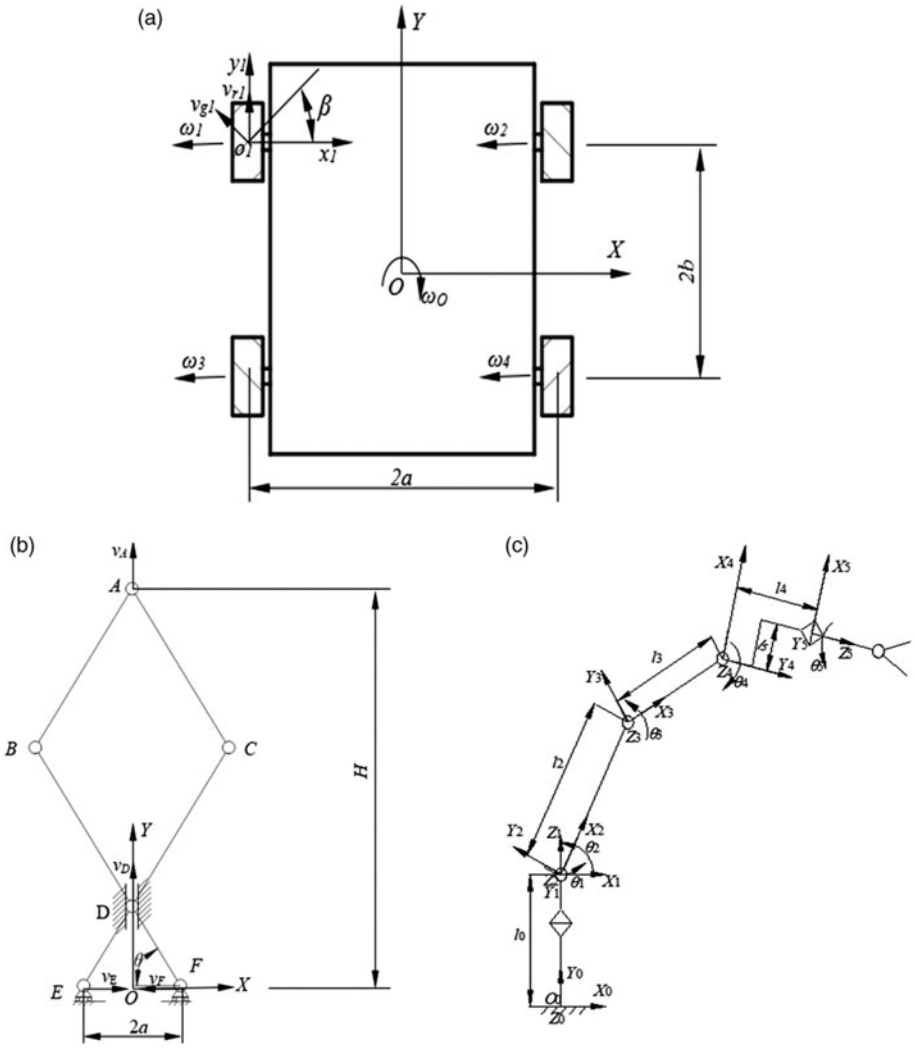


Fig. 6. Mcnum wheel layout sketch.

The motion of point O_1 in the coordinate O-XY is written as

$$\begin{bmatrix} v_{o_1X} \\ v_{o_1Y} \end{bmatrix} = \begin{bmatrix} 1 & 0 & b \\ 0 & 1 & a \end{bmatrix} \begin{bmatrix} v_X \\ v_Y \\ \omega_O \end{bmatrix} \tag{11}$$

From Equations (10) and (11), we can compute

$$\omega_1 = \frac{1}{R} [\cot\beta \quad 1 \quad b\cot\beta + a] \begin{bmatrix} v_X \\ v_Y \\ \omega_O \end{bmatrix} \tag{12}$$

Similarly, the remaining three wheels of motion are in the same form as wheel 1, and the inverse kinematics equation is

$$\begin{bmatrix} \omega_1 \\ \omega_2 \\ \omega_3 \\ \omega_4 \end{bmatrix} = \frac{1}{R} \begin{bmatrix} \cot\beta & 1 & b\cot\beta + a \\ -\cot\beta & 1 & -b\cot\beta - a \\ -\cot\beta & 1 & b\cot\beta + a \\ \cot\beta & 1 & -b\cot\beta - a \end{bmatrix} \begin{bmatrix} v_X \\ v_Y \\ \omega_O \end{bmatrix} \tag{13}$$

https://doi.org/10.1017/S0263574720000740 Published online by Cambridge University Press

Table III. Manipulator D-H parameters.

i	α_{i-1}	a_{i-1}	d_i	θ_i
1	−90°	0	l_0	θ_1
2	90°	0	0	θ_2
3	0°	l_2	0	θ_3
4	180°	l_3	0	θ_4
5	0°	l_5	l_4	θ_5

Substituting geometric quantity $\beta = 45°$ into Eq. (11), we get

$$\begin{bmatrix} \omega_1 \\ \omega_2 \\ \omega_3 \\ \omega_4 \end{bmatrix} = \frac{1}{R} \begin{bmatrix} 1 & 1 & b+a \\ -1 & 1 & -b-a \\ -1 & 1 & b+a \\ 1 & 1 & -b-a \end{bmatrix} \begin{bmatrix} v_X \\ v_Y \\ \omega_O \end{bmatrix} \tag{14}$$

The rank $R(K) = 3$ of matrix K is obtained, so it is known that when the motion speed of the robot body is known, the angular velocity of the four motor can be obtained, $\omega 1$, $\omega 2$, $\omega 3$, and $\omega 4$, and on the contrary, the angular velocity of the motor is also obtained by the motion speed of the robot body, which is

$$\begin{bmatrix} v_X \\ v_Y \\ \omega_O \end{bmatrix} = \frac{R}{4} \begin{bmatrix} 1 & -1 & -1 & 1 \\ 1 & 1 & 1 & 1 \\ \dfrac{1}{b+a} & \dfrac{1}{-b-a} & \dfrac{1}{b+a} & \dfrac{1}{-b-a} \end{bmatrix} \begin{bmatrix} \omega_1 \\ \omega_2 \\ \omega_3 \\ \omega_4 \end{bmatrix} \tag{15}$$

Substituting robot geometry dimensions $R = 0.05$ m, $a = 0.26$ m, $b = 0.22$ m into Eq. (15), we can compute

$$\begin{bmatrix} v_X \\ v_Y \\ \omega_O \end{bmatrix} = \begin{bmatrix} 0.0125 & -0.0125 & -0.0125 & 0.0125 \\ 0.0125 & 0.0125 & 0.0125 & 0.0125 \\ \dfrac{5}{92} & -\dfrac{5}{92} & \dfrac{5}{192} & -\dfrac{5}{192} \end{bmatrix} \begin{bmatrix} \omega_1 \\ \omega_2 \\ \omega_3 \\ \omega_4 \end{bmatrix} \tag{16}$$

The four-bar lifting mechanism is a symmetrical structure, and its structure diagram is shown in Fig. 6(b), which can be obtained as

$$v_H = -\frac{25}{2\pi} \omega_M \cot\theta \tag{17}$$

It shows that the lifting speed of the four-bar lifting mechanism v_H is related to the speed of the motor ω_M and the angle θ between the BF of the lifting rod and the negative direction of the X axis.

In this paper, the manipulator is a component of a nuclear power inspection robot that performs operations, with five degrees of freedom, its D-H model is shown in Fig. 6(c), and the parameters are shown in Table III.

The transformation matrix[14] of the manipulator can be obtained by multiplying the T matrix of each adjacent joint as

$${}^0T_5 = {}^0T_1(\theta_1) \cdot {}^1T_2(\theta_2) \cdot {}^2T_3(\theta_3) \cdot {}^3T_4(\theta_4) \cdot {}^4T_5(\theta_5) \tag{18}$$

https://doi.org/10.1017/S0263574720000740 Published online by Cambridge University Press

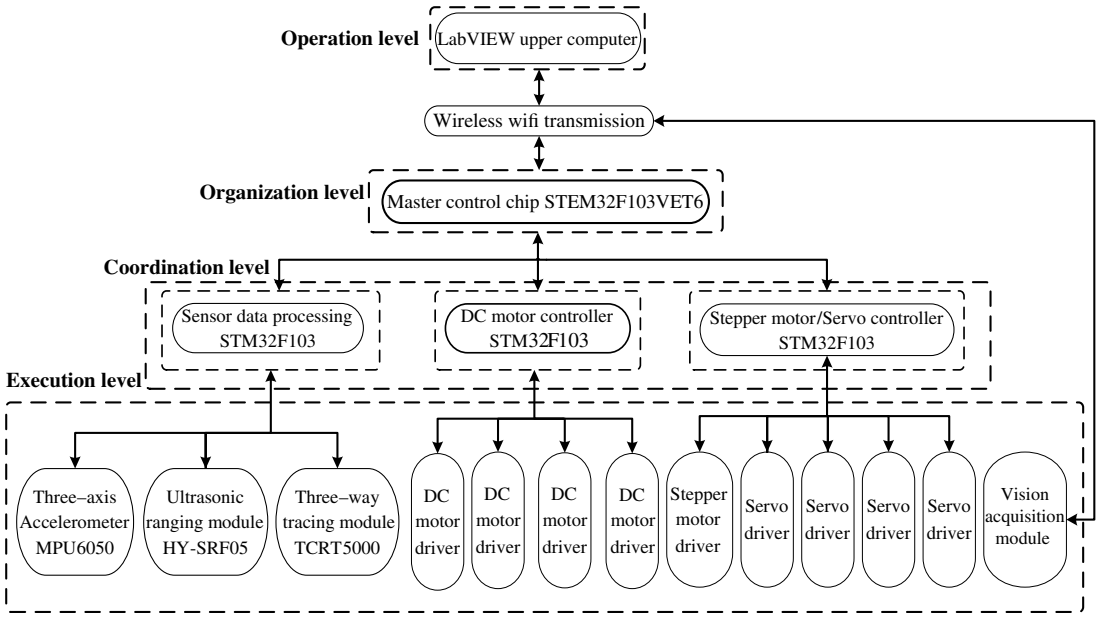


Fig. 7. Control route diagram.

Substituting the rotation angles and end local coordinates of each joint into Eq. (18) yields the position and pose of the end effector of the manipulator.

$$\begin{aligned}
x &= l_2^*\mathrm{c}(\theta_1)^*\mathrm{c}(\theta_2) - l_5^*(\mathrm{c}(\theta_4)^*(\mathrm{c}(\theta_1)^*\mathrm{s}(\theta_2)^*\mathrm{s}(\theta_3) - \mathrm{c}(\theta_1)^*\mathrm{c}(\theta_2)^*\mathrm{c}(\theta_3)) - \mathrm{s}(\theta_4)^*(\mathrm{c}(\theta_1)^*\mathrm{c}(\theta_2)^*\mathrm{s}(\theta_3) \\
&\quad + \mathrm{c}(\theta_1)^*\mathrm{c}(\theta_3)^*\mathrm{s}(\theta_2))) - l_4^*\mathrm{s}(\theta_1) - z_5^*\mathrm{s}(\theta_1) - l_3^*(\mathrm{c}(\theta_1)^*\mathrm{s}(\theta_2)^*\mathrm{s}(\theta_3) - \mathrm{c}(\theta_1)^*\mathrm{c}(\theta_2)^*\mathrm{c}(\theta_3)) \\
y &= l_0 + l_3^*(\mathrm{c}(\theta_2)^*\mathrm{s}(\theta_3) + \mathrm{c}(\theta_3)^*\mathrm{s}(\theta_2)) + l_2^*\mathrm{s}(\theta_2) + l_5^*(\mathrm{c}(\theta_4)^*(\mathrm{c}(\theta_2)^*\mathrm{s}(\theta_3) + \mathrm{c}(\theta_3)^*\mathrm{s}(\theta_2)) \\
&\quad - \mathrm{s}(\theta_4)^*(\mathrm{c}(\theta_2)^*\mathrm{c}(\theta_3) - \mathrm{s}(\theta_2)^*\mathrm{s}(\theta_3))) \\
z &= l_3^*(\mathrm{s}(\theta_1)^*\mathrm{s}(\theta_2)^*\mathrm{s}(\theta_3) - \mathrm{c}(\theta_2)^*\mathrm{c}(\theta_3)^*\mathrm{s}(\theta_1)) + l_5^*(\mathrm{c}(\theta_4)^*(\mathrm{s}(\theta_1)\mathrm{s}(\theta_2)^*\mathrm{s}(\theta_3) - \mathrm{c}(\theta_2)^*\mathrm{c}(\theta_3)^*\mathrm{s}(\theta_1)) \\
&\quad - \mathrm{s}(\theta_4)^*(\mathrm{c}(\theta_2)^*\mathrm{s}(\theta_1)^*\mathrm{s}(\theta_3) + \mathrm{c}(\theta_3)^*\mathrm{s}(\theta_1)^*\mathrm{s}(\theta_2))) - l_4^*\mathrm{c}(\theta_1) - z_5^*\mathrm{c}(\theta_1) - l_2^*\mathrm{c}(\theta_2)^*\mathrm{s}(\theta_1) \qquad (19)
\end{aligned}$$

where c is cos and s is sin. Based on Eq. (19), the each joint angle of the manipulator can be obtained by the inverse kinematics, which is unnecessary to go into details here.

4. Robot Control Design

The robot control system adopts a hierarchical control strategy in which the remote control mode of the upper computer is realized by Labview control interface, the lower computer is composed of organization level, coordination level, and execution level, and the wireless wifi transmission is selected by the upper and lower computer communication modes. The overall technical route is shown in Fig. 7.

4.1. Walking motor control of fuzzy adaptive PID

In MATLAB, the rules of fuzzy controller are formulated, the fuzzy rules are called under the Simulink module, the fuzzy variables of fuzzy control can be obtained, and the membership function of each input and output is obtained by using the method of triangular membership function.[15–17] The rule table obtained by establishing the fuzzy control rules is shown in Fig. 8.

In the Simulink program of MATLAB, a block diagram of traditional Proportional Integral Derivative (PID) and fuzzy adaptive PID is established, which is shown in Fig. 9, and the simulation results of output response following input step signal are obtained.

In the case of step input, the setting steady-state value error is 0.3%, the simulation results show that the adjustment time to reach the steady-state value is only 0.2 s, the fuzzy adaptive PID control has the ability of fast response, and the maximum overshoot of the system is about 2%. In the adjustment time, the oscillation times of fuzzy adaptive PID are much smaller than those of traditional PID,

https://doi.org/10.1017/S0263574720000740 Published online by Cambridge University Press

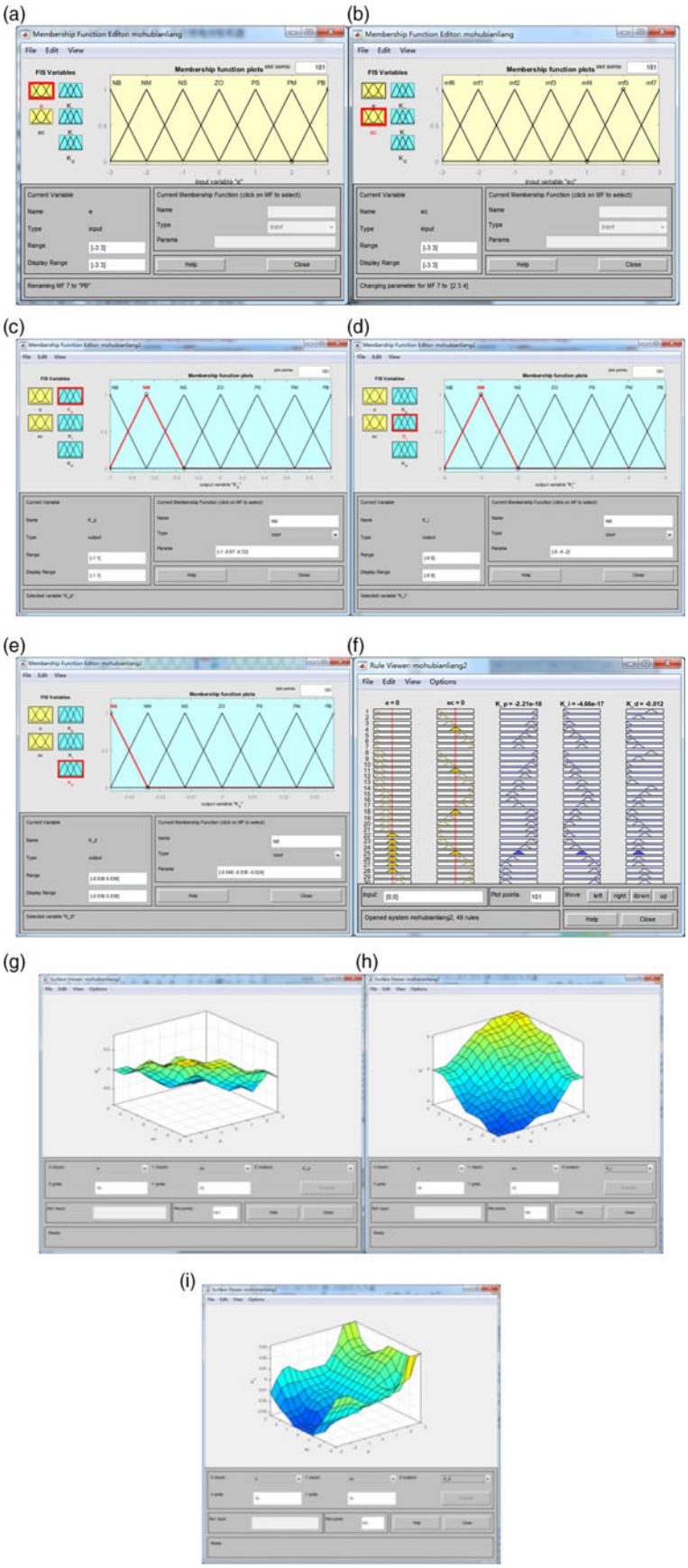


Fig. 8. Fuzzy rules. (a) The membership function of e. (b) The membership function of ec. (c) The membership function of $\triangle Kp$. (d) The membership function of $\triangle K_i$. (e) The membership degree of $\triangle K_d$. (f) Fuzzy control rule table. (g) $\triangle K_p$ rule. (h) $\triangle K_i$ rule. (i) $\triangle K_d$ rule.

https://doi.org/10.1017/S0263574720000740 Published online by Cambridge University Press

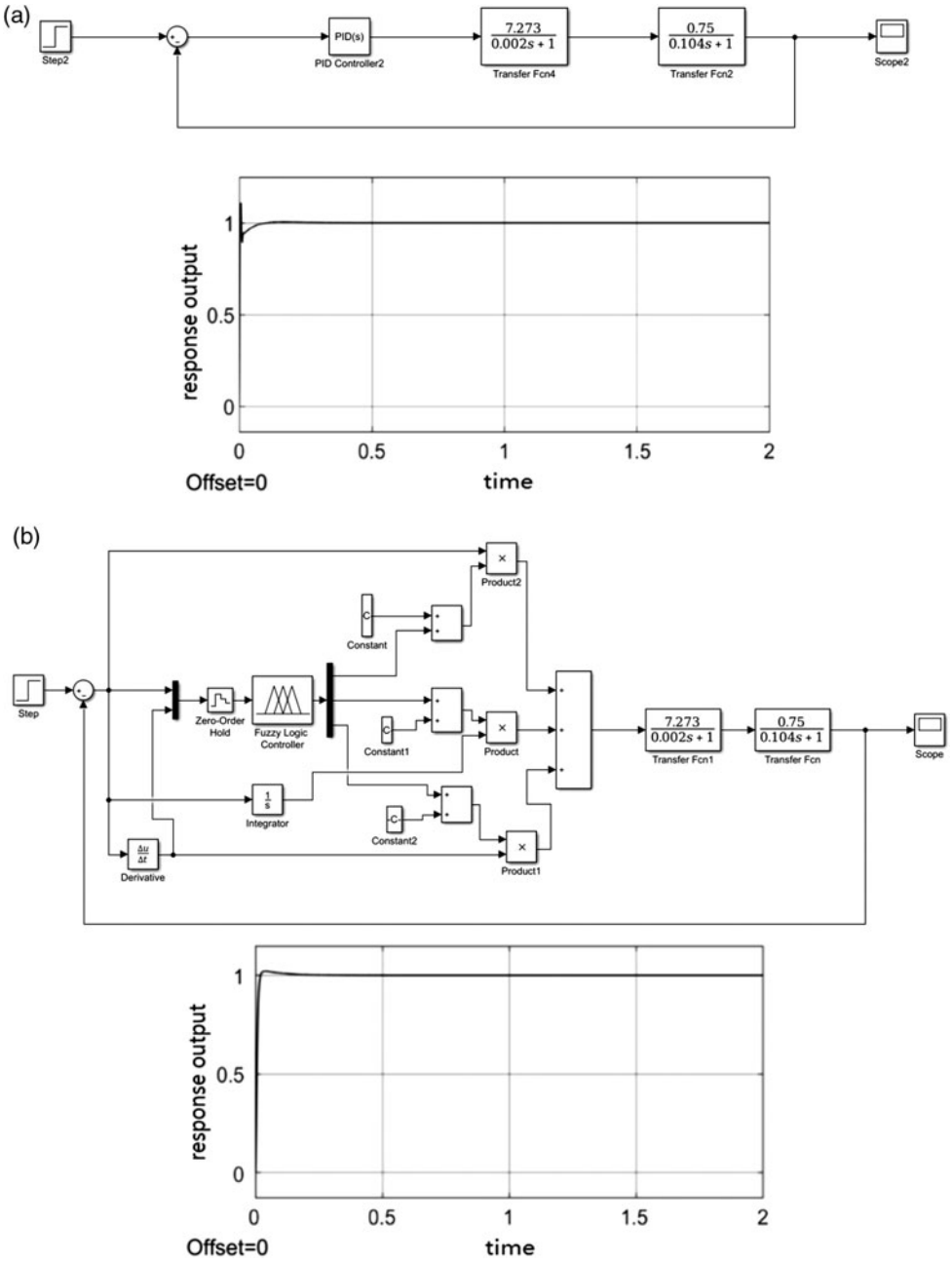


Fig. 9. Program block diagram and simulation results of fuzzy adaptive PID. (a) Traditional PID simulation. (b) Fuzzy adaptive PID simulation.

and the maximum overshoot is smaller than that of traditional PID, which has strong robustness and stability, and verifies the feasibility of fuzzy adaptive PID control algorithm.

4.2. Lifting drive control

The acceleration and deceleration of the lifting drive motor can be r controlled by using the seven-segment S-curve algorithm to reduce the vibration and noise impact. In the seven-segment S-curve algorithm, it is divided into seven stages, plus acceleration, uniform acceleration, reduction acceleration, uniform speed, acceleration and deceleration, uniform deceleration, and deceleration reduction, which are shown in Fig. 10.

To simplify the control program, set the time interval for acceleration, uniform acceleration, and reduction acceleration to equal, that is, $t_1 = t_2 - t_1 = t_3 - t_2$, and then the maximum speed $\omega(t_3)$ can be expressed as

https://doi.org/10.1017/S0263574720000740 Published online by Cambridge University Press

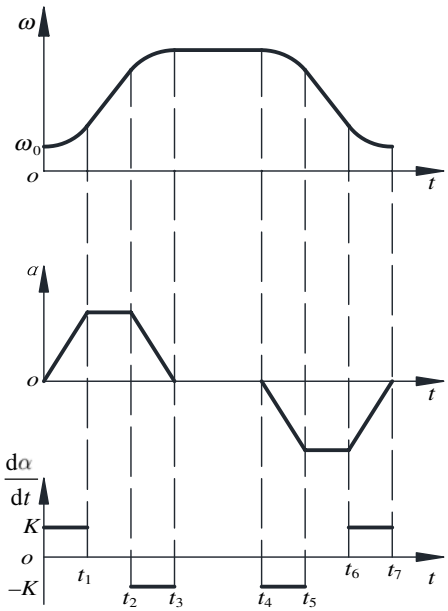


Fig. 10. Seven-segment *S*-curve.

$$\omega(t_3) = \omega_0 + \frac{1}{2}Kt_1^2 + Kt_1(t_2 - t_1) + Kt_1(t_3 - t_2) - \frac{1}{2}K(t_3 - t_2)^2 = \omega_0 + 2Kt_1^2 \tag{20}$$

Eq. (21) is as follows:

$$\begin{cases} \theta = \omega_0 t_7 + Kt_1^2\,(\Delta t + t_7) \\ t_7 = 6t_1 + \Delta t \\ \omega_0 + 2Kt_1^2 \le 4\pi \\ t_1 > 0 \\ \Delta t \ge 0 \\ 0 < t_7 \le 4 \end{cases} \tag{21}$$

where $\omega_0 = 0$, $K = 100$, $\Delta t = t4 - t3$, $\Delta t = 0$, $t7 = 6t1$, as $t1 = \sqrt{\frac{\pi}{50}}$, $\omega_{\max} = 2$ r/s, and there is $\theta = 200t_1^2 t_7 - 600t_1^3 = 9.45$rad

$$t_1 = \begin{cases} \sqrt[3]{\dfrac{\theta}{600}} & 0 < \theta < 9.45 \\ \sqrt{\dfrac{\pi}{50}} & \theta \ge 9.45 \end{cases} \quad ; \quad t_7 = \begin{cases} 6\sqrt[3]{\dfrac{\theta}{600}} & 0 < \theta < 9.45 \\ \dfrac{\theta}{4\pi} + \sqrt{\dfrac{9\pi}{50}} & \theta \ge 9.45 \end{cases}$$

$$\Delta t = t_7 - 6t_1 = \frac{\theta}{4\pi} - \sqrt{\frac{9\pi}{50}}$$

Based on Eq. (21), we can get the time at which the drive mechanism reaches any height.

5. Robot Experiments

The physical object of nuclear power inspection robot and computer LabVIEW control interface are shown in Fig. 11. Experiments are carried out on nuclear power inspection robot, including robot walking control experiment, lifting function experiment and operation experiment.

5.1. Walking control experiment

Using LabVIEW upper computer to send the control instruction with three axis directions speed information to the organization-level master chip through the serial transfer WiFi module. After receiving the instruction, the master chip is issued to the coordinated level walking control chip, and

https://doi.org/10.1017/S0263574720000740 Published online by Cambridge University Press

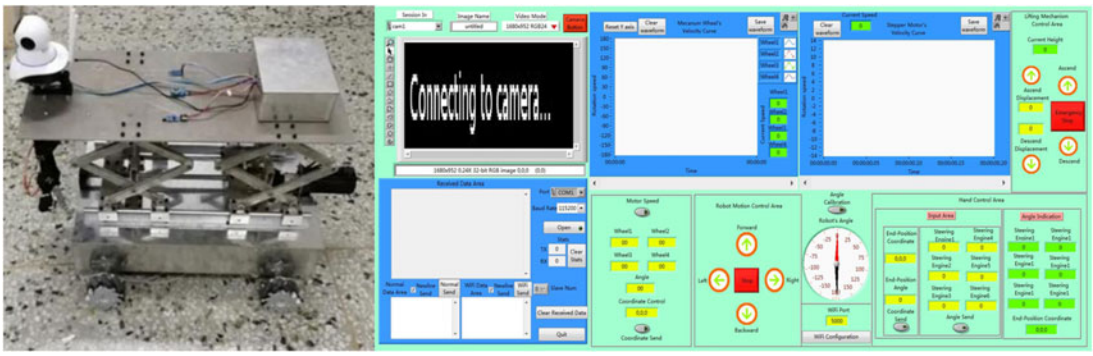


Fig. 11. Robot physical diagram and LabVIEW interface.

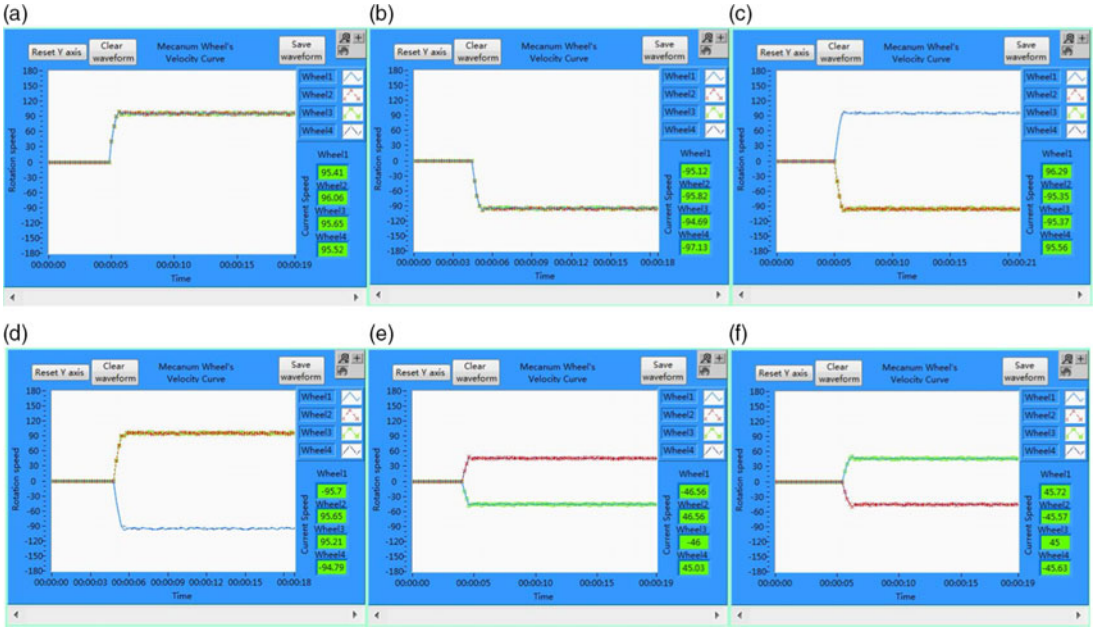


Fig. 12. Walking control experiment of nuclear power inspection robot. (a) Forward speed curve. (b) Backward speed curve. (c) Left shift speed curve. (d) Right shift speed curve. (e) Clockwise rotation speed curve. (f) Counterclockwise rotation speed curve.

the walking control chip is converted to obtain the speed of each mcnum wheel, which is then sent to the execution level, driving the robot to walk. In the process of motion, the fuzzy adaptive PID controller is used to adjust the speed of each wheel, and the rotational speed waveform collected by the upper computer is shown in Fig. 12.

Experiments show that the mcnum wheel can quickly respond to the upper computer instructions, and when the motion is controlled, the motor can output the stable speed well. Although there are small differences between mcnum wheels, it may be due to the uneven manufacturing process and ground surface of each mcnum wheel, which can be continuously corrected during walking to meet the expected requirements.

5.2. Lifting function experiment

Using LabVIEW upper computer, we can send the lifting control height instructions to the organization-level master chip through the serial transfer WiFi module. After receiving the instruction, the master chip is issued to the coordinated-level lifting control chip, and the lifting control chip calculates the time point of each seven-segment S-curve by height and converts it into pulse information, which is then sent to the lifting execution level to drive the lifting mechanism. The speed waveforms captured by the upper computer are given in Fig. 13, which shows that there is no impact on the lifting.

https://doi.org/10.1017/S0263574720000740 Published online by Cambridge University Press

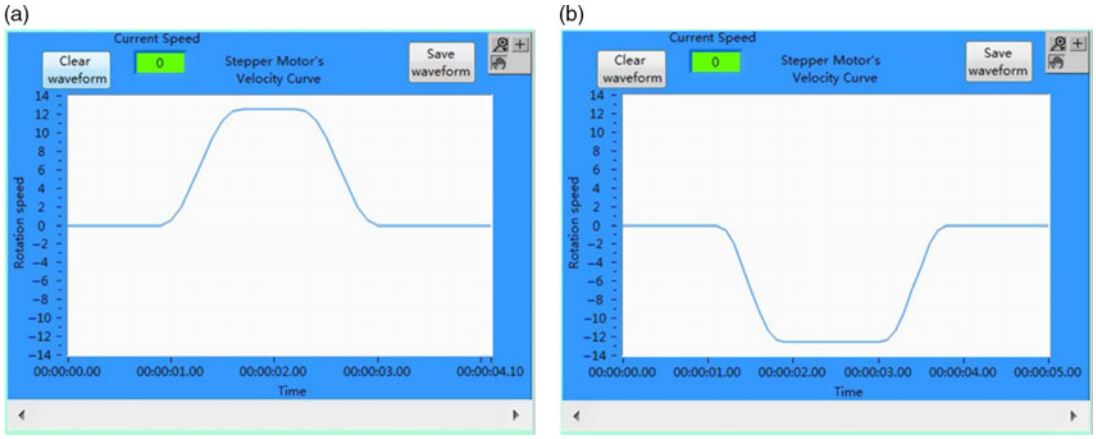


Fig. 13. Lifting drive speed diagram. (a) Upward velocity measurement curve. (b) Downward velocity measurement curve.

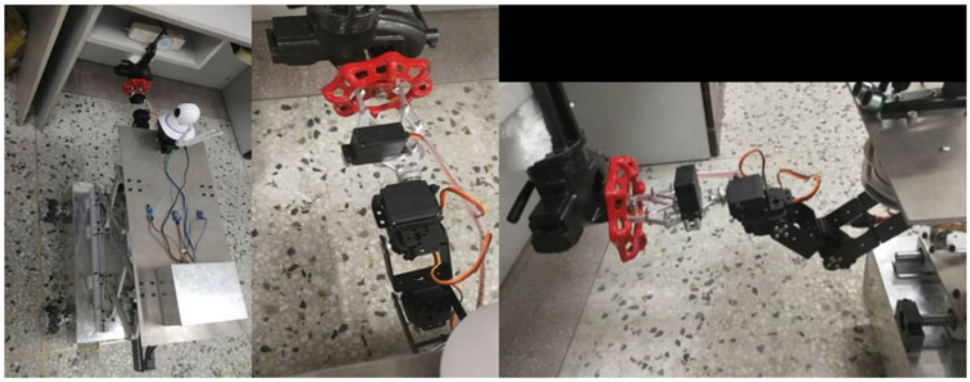


Fig. 14. Manipulator operation experiment.

5.3. Manipulation experiment

Using LabVIEW upper computer, we can send the manipulation control valve position and manipulator end position and pose instructions to the organization-level master chip through the serial transfer WiFi module. After receiving the instruction, the master chip is issued to the coordinated-level manipulator control chip. The trigger manipulator operation action is shown in Fig. 14.

6. Conclusions

The paper has developed a small and lightweight nuclear power plant inspection robot; meanwhile, the mechanical analysis, structure statics analysis, motion equation establishment, and robot system control all have been done. Based on the design and comprehensive experimental research on nuclear power inspection robot which is useful for engineering design and control strategy of a certainly of robot system, the following conclusions are drawn.

(1) In this paper, a nuclear power inspection robot with the lightweight main structure design is developed, which meets the strength requirement. The configuration of the function module is completed, and the functions of each module are clear, which is convenient for robot programming control and expansion function.
(2) The kinematics equations of walking mechanism, lifting mechanism, and manipulator are established, respectively, which lays a foundation for robot motion control.
(3) The hierarchical lower computer control and the control system based on LabVIEW upper computer of the robot are designed. The fuzzy PID method is used to control the robot walking motion, which has good control effect.
(4) Using wireless Wifi communication mode, the robot is operated remotely, and the experimental verification of nuclear power inspection robot is completed including walking experiment, lifting

https://doi.org/10.1017/S0263574720000740 Published online by Cambridge University Press

experiment, and operation experiment, and the experimental results verify that the LabVIEW upper computer can meet the remote control function requirements of nuclear power inspection robot.

References

1. C. Y. Ma, H. B. Gao, L. Ding, J. G. Tao, K. R. Xia, H. T. Yu and Z. Q. Deng, "Optimal energy consumption for mobile manipulators executing door-opening task," *Math. Prob. Eng.* **2018**, 1–11 (2018).
2. L. E. Reinerman-Jones, N. Hughes, A. D'Agostino and G. Matthews, "Human performance metrics for the nuclear domain: A tool for evaluating measures of workload, situation awareness and teamwork," *Int. J. Ind. Ergon.* **69**, 217–227 (2019).
3. L. Waganer, C. Kessel, S. Malang, E. Marriott, S. Reyes and A. Davis, "The examination of the FNSF maintenance approach," *Fusion Eng. Des.* **135**(SI), 394–425 (2018).
4. C. Ducros, G. Hauser, N. Mahjoubi, P. Girones, L. Boisset, A. Sorin, E. Jonquet, J. M. Falciola and A. Benhamou, "RICA: A tracked robot for sampling and radiological characterization in the nuclear field," *J. Field Robot.* **34**(3), 583–599 (2017).
5. H. Li, B. Li and W. F. Xu, Development of a Remote-Controlled Mobile Robot with Binocular Vision for Environment Monitoring," *IEEE International Conference on Information and Automation 2015, AUG8-10* (2015) pp. 737–742.
6. H. Shin, Y. Bae, S. Jung, Y. Choi and C. Kim, "Development of a Remote Steel Pipe Cutting Robot System," *15th International Conference on Ubiquitous Robots (UR)* (2018) pp. 103–107.
7. J. H. Kim, "Reactor nozzle inspection based on the laser-guided mobile robot," *Int. J. Adv. Robot. Syst.* **15**(1), 1–13 (2018).
8. R. A. Iureva and A. S. Timko, "Radiation-Resistant Television System for Articulated Manipulator Arm," *Conference on Optical Design and Engineering VII* (10690):106901Q1-6 (2019).
9. A. Krishnan, V. Thejus and B. M. Arjun, "Numerical Investigation of Structural Design of Torsion Links in a Landing Gear Retraction Mechanism," *2nd International Conference for Convergence in Technology (I2CT), APR 07-09* (2017) pp. 382–388.
10. J. Wu and Q. Wang, "Finite Element Analysis of New Crankshaft Automatic Adjustment Mechanism of Pumping Unit," *IOP Conference Series-Materials Science and Engineering*, vol. 274 (2017) pp. 1–14.
11. Y. F. Zheng, Y. M. Hu, B. Wu, P. X. Yi and J. Liu, "Finite Element Modal Analysis of Four-link Combination Portal Crane," *3rd International Conference on Mechatronics, Robotics and Automation(ICMRA), APR20-21* (2015) pp. 662–665.
12. J. S. Keek, S. L. Loh and S. H. Chong, "Comprehensive development and control of a path-trackable Mecanum-Wheeled robot," *IEEE Access* **7**, 18368–18381 (2019).
13. S. R. Sahoo, S. S. Chiddarwar and V. Alakshendra, "Intuitive dynamic modeling and flatness-based nonlinear control of a mobile robot," SIMULATION: Transactions of The Society for Modeling and Simulation International **94**(9), 797–820 (2018).
14. R. Arora, D. Agarwal and T. K. Bera, "Workspace analysis and trajectory tracking of a planar hybrid manipulator with ball screw feed drive," *J. Brazilian Soc. Mech. Sci. Eng.* **41**(9), 1–18 (2019).
15. U. M. Nath, C. Dey and R. K. Mudi, "Fuzzy tuned model based control for level and temperature processes," *Microsyst. Tech. Micro Nanosyst. Inf. Storage Process. Syst.* **25**(3), 819–827 (2019).
16. S. Dettori, V. Iannino, V. Colla and A. Signorini, "An adaptive Fuzzy logic-based approach to PID control of steam turbines in solar applications," *Appl. Energy* **227**(SI), 655–664 (2018).
17. A. K. D. Velayudhan, "Design of a supervisory fuzzy logic controller for monitoring the inflow and purging of gas through lift bags for a safe and viable salvaging operation," *Ocean Eng.* **171**, 193–201 (2019).

https://doi.org/10.1017/S0263574720000740 Published online by Cambridge University Press